Journal of
**Applied Crystallography**
ISSN 0021-8898

Received 21 September 2005
Accepted 13 March 2006

# The instrumental resolution function of synchrotron radiation powder diffractometers in the presence of focusing optics

**Fabia Gozzo,[a]* Liberato De Caro,[b] Cinzia Giannini,[b] Antonietta Guagliardi,[b] Bernd Schmitt[a] and Andrea Prodi[a]**

[a]Swiss Light Source, Paul Scherrer Institute, CH-5232 Villigen PSI, Switzerland, and [b]Institute of Crystallography (IC-CNR), Via Amendola 122/0, 70126 Bari, Italy. Correspondence e-mail: fabia.gozzo@psi.ch

The theory developed by Caglioti and co-workers [Caglioti, Paoletti & Ricci (1958). *Nucl. Instrum.* **3**, 223–228; Caglioti, Paoletti & Ricci (1960). *Nucl. Instrum. Methods*, **9**, 195–198; Caglioti & Ricci (1962). *Nucl. Instrum. Methods*, **15**, 155–163] and Sabine [(1987). *J. Appl. Cryst.* **20**, 23–27, 173–178] that provides an analytical description of the instrumental resolution function of single-crystal and powder diffractometers consisting of sequences of collimators and crystals is extended by including the effect of collimating and refocusing mirrors. A simple analytical expression with only two fitting parameters (the beam divergence after reflection by the collimating and the refocusing mirrors) is determined, this expression being applicable to all mirror settings. The new theory is applied to experimental data collected at the Swiss Light Source Materials Science beamline powder diffractometer for three photon energies under extreme mirror bending conditions using the small-linewidth powder sample $Na_2Ca_3Al_2F_{14}$.



## 1. Introduction

Between 1958 and 1962, Caglioti, Paoletti and Ricci published three fundamental papers describing how to construct, on the basis of a Gaussian approximation, analytical expressions for the instrumental resolution function (IRF) of single-crystal and powder neutron diffractometers consisting of sequences of collimators and monochromator crystals (Caglioti *et al.*, 1958, 1960; Caglioti & Ricci, 1962). Sabine (1987) extended this work to synchrotron optical systems consisting of alternate collimators and reflecting crystals. Several other studies have been devoted to the determination of the instrumental resolution and the profile shape functions (Hastings *et al.*, 1984; Cox *et al.*, 1988; Cox, 1991; Langford *et al.*, 1991, Scardi *et al.*, 1996; Balzar *et al.*, 1997; Masson, Dooryhée *et al.*, 2001; Masson, Guinebretiere *et al.*, 2001). More recently, Masson *et al.* (2003) proposed a new theoretical approach, which consists of generating the instrumental profile through the convolution of angle-independent aberration functions, whose analytical form can be of any kind. The method is very general and, therefore, applicable to any synchrotron optical system. However, this approach does not generate simple analytical expressions and, therefore, is not ideal for simulating instrumental functions to define quickly the optimum optical parameters for a given experiment or detect irregularities in the instrument performance, in particular for optical systems with focusing optics that can be set very differently depending on the degree of bending of the mirrors.

In this article, we further develop Sabine's work by including the effect of collimating and refocusing X-ray mirrors on the overall instrumental resolution function and formulate a simple analytical expression under the same Gaussian approximation. Experimental evidence that justifies the legitimacy of the approximation is also provided. The theoretical study presented in this article specifically applies to the optical setting at the Swiss Light Source Materials Science (SLS-MS) beamline powder diffraction station. However, the formulation is performed in such a way that the reader can easily adapt it to describe any optical setting consisting of single crystals, collimators and collimating/refocusing X-ray mirrors. In §2, we briefly recall Sabine's expression for the total reflection probability and the FWHM (full width at half-maximum) for a powder diffractometer, a double-crystal monochromator and an analyzer crystal on the counter arm, and in §3, we extend Sabine's expression to include the effect of the collimating and refocusing mirrors on the overall IRF. In §4, we describe how to determine the widths $\Delta\tau'_p$ and $\Delta\tau'_f$ of the beam divergence probability distribution functions after reflection by the first collimating and the second focusing X-ray mirrors, taking into account the effects arising from incorrect and/or approximated mirror curvatures, and we derive the analytical expression of collimator-like terms

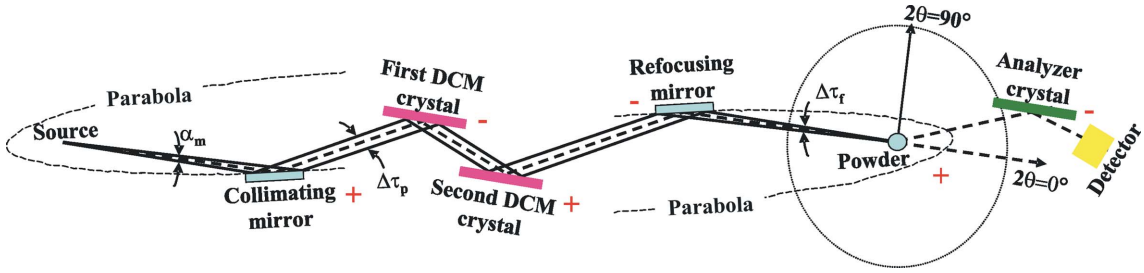


**Figure 1**
High-resolution optical setting at the Swiss Light Source Materials Science beamline powder diffraction station described in the text.

appearing in the extended Sabine-like expression, using the Liouville theorem. A detailed theoretical derivation of $\Delta\tau'_p$ and $\Delta\tau'_f$ has been deposited as supplementary information.[1] In §5, we analyze the effect of additional contributions influencing the IRF, and in §6, using our model we simulate theoretical IRFs as a function of relevant experimental parameters. In §7, we apply our model to experimental data collected at the SLS-MS beamline powder diffractometer at three different photon energies using $Na_2Ca_3Al_2F_{14}$ (NAC) powder (Courbion & Ferey, 1988) and discuss the results. A brief description of the powder station and the experiments is also provided. Finally, in §8 we draw our conclusions.

## 2. Sabine's expression for a powder diffractometer, a double-crystal monochromator and an analyzer crystal on the counter arm

The case of a powder diffractometer, a double-crystal monochromator (DCM) and an analyzer crystal on the counter arm can be easily obtained from the four-crystal spectrometer in setting (1, −1, 1, −1) by assuming that the powder sample behaves as a single crystal with an infinite mosaic spread [Sabine (1987), p. 26, equation (9)]. The total reflection probability $I(\beta)$ has, therefore, the following expression:

$$I(\beta) = \int\int \mathrm{d}\alpha\,\mathrm{d}\delta \exp -\left[\left(\frac{\alpha}{\alpha'_m}\right)^2 + 2\left(\frac{\delta-\alpha^2}{\Delta'_m}\right) + \left(\frac{b\delta+\alpha-\beta}{\Delta'_a}\right)^2\right], \quad (1)$$

with

$$b = \tan\theta_a/\tan\theta_m - 2\tan\theta/\tan\theta_m.$$

In equation (1), $\alpha'_m$ denotes the width of the vertical beam divergence probability distribution function, $\Delta'_m$ and $\Delta'_a$ are the widths of the monochromator and the analyzer crystal mosaic block probability distribution functions (or Darwin widths), and $\delta = \theta - \theta_m$ is the difference between the monochromator Bragg angles of an individual ($\theta$) and the central ($\theta_m$) ray. The angle $\beta$ takes into account the finite detector acceptance. The integration in equation (1) over $\alpha$ and $\delta$ between $-\infty$ and $+\infty$ leads to an analytical expression for the IRF, whose FWHM is given[2] by

$$\Delta^2(2\theta) = \alpha_m^2\left(1 + \tan\theta_a/\tan\theta_m - 2\tan\theta/\tan\theta_m\right)^2 + \Delta_m^2\left(\tan\theta_a/\tan\theta_m - 2\tan\theta/\tan\theta_m\right)^2/2 + \Delta_a^2. \quad (2)$$

In this article, we derive a more general expression that includes the contribution of the two collimating and refocusing X-ray parabolic mirrors to the overall IRF. The reflection probabilities are built up as products of exponential terms, according to the general Caglioti–Paoletti–Ricci and Sabine approach. The ultra-high-resolution case, corresponding to a collimating first mirror and a flat second mirror to produce a parallel incident beam on the sample, is here treated as a limiting case of a collimating mirror, for which only the effects of gravity and thermal deformation are relevant.

## 3. Sabine-like IRF expression in the presence of parabolic collimating and refocusing mirrors

Fig. 1 describes the SLS-MS beamline powder diffraction optics consisting of a wiggler source, a collimating mirror, an Si(111) DCM, a refocusing mirror and an analyzer Si(111) crystal following the powder sample. In the Debye–Scherrer geometry, the optical configuration in the vertical diffraction plane is therefore (1, −1, 1, −1, 1, −1). Referring to Fig. 1, when the first mirror is bent into an ideal parabola, a beam of divergence $\alpha_m$ from a point-like source in the focal point becomes, after being reflected by the first collimating mirror, a nominally perfect parallel beam. It is then monochromated by the DCM and refocused by the second parabolic mirror to a focal point, where the sample is located. In reality, even ignoring manufacturing mirror imperfections, a departure from the ideal collimating and refocusing conditions always occurs as a result of finite source size, optical aberrations (in particular coma and spherical aberrations; Susini, 1995; Howells, 1994) and approximations performed when shaping the mirror (*e.g.* symmetric *versus* asymmetric bending). The departure from ideal conditions changes the probability of the photon being reflected as a function of the local incidence angle, which, in turn, is a function of the photon energy. Let

[1] Supplementary material has been deposited in the IUCr electronic archives (Reference: HX5036). Services for accessing this material are described at the back of the journal.

[2] Note that in IRF equations the FWHMs $\Delta_i$, $\alpha_i$ always replace the corresponding distribution function widths $\Delta'_i$, $\alpha'_i$ that appear in the probability expressions.

$\Delta\tau'_{\rm p}$ and $\Delta\tau'_{\rm f}$ be the widths of the beam divergence Gaussian distribution functions after reflection by the first and second bent parabolic mirrors. Under ideal conditions and one-to-one focusing optics (magnification equal to one), $\Delta\tau'_{\rm p}$ should be zero (perfectly collimated beam) and $\Delta\tau'_{\rm f}$ should be equal to the source vertical divergence $\alpha'_{\rm m}$. In §4, we describe the derivation of analytical expressions for $\Delta\tau'_{\rm p}$ and $\Delta\tau'_{\rm f}$ in the case of real parabolic mirrors (Susini, 1995) in order to determine their best estimate for the specific system under investigation when these quantities are not already known. We observe that, at the SLS Materials Science beamline, the mirrors' grazing incident angles are changed as a function of energy (above 10 keV photon energy) according to an empirical algorithm that is also implemented in our model (Patterson *et al.*, 2005).

We need now to formulate appropriate expressions for the terms to be added to Sabine's equation (1); these terms describe the presence of collimating and refocusing mirrors. Since the mirrors essentially affect the vertical beam divergence, we can formally treat them as collimators, but we additionally take into account that

(i) a mirror changes the degree of collimation of the beam according to Liouville's theorem (Arndt, 1990);

(ii) the beam direction is inverted after reflection.

Thus, for the total probability $I(\beta)$ of a photon being reflected by all the optical elements in Fig. 1 and finally being detected, we therefore write

$$I(\beta) = \int\int\int\int \mathrm{d}\alpha\,\mathrm{d}\delta\,\mathrm{d}\eta\,\mathrm{d}\gamma \exp -\left[\left(\frac{\alpha}{\alpha'_{\rm m,effective}}\right)^2 + \left(\frac{2\eta-\alpha}{\Delta\tau'_p}\right)^2 + 2\left(\frac{\delta-(2\eta-\alpha)}{\Delta'_{\rm m}}\right)^2 + \left(\frac{-(2\eta-\alpha)+2\gamma-\alpha}{\Delta\tau'_{\rm f,effective}}\right)^2 + \left(\frac{b\delta-(2\eta-\alpha)+2\gamma-\alpha+\beta}{\Delta'_{\rm a}}\right)^2\right], \quad (3)$$

with

$$b = \tan\theta_{\rm a}/\tan\theta_{\rm m} - 2\tan\theta/\tan\theta_{\rm m},$$

$$\alpha'_{\rm m,effective} \cong \begin{cases} \alpha'_{\rm m} & \text{if the mirror angular acceptance} \geq \text{the source divergence} \\ \alpha'_{\rm c} & \text{if the mirror angular acceptance} < \text{the source divergence} \end{cases} \quad (4a)$$

$$\Delta\tau'_{\rm f,effective} \cong \begin{cases} \Delta\tau'_{\rm f} & \text{if the sample size (or the slit width)} \geq \text{the spot size} \\ \Delta'_{\rm s} & \text{if the sample size (or the slit width)} < \text{the spot size.} \end{cases} \quad (4b)$$

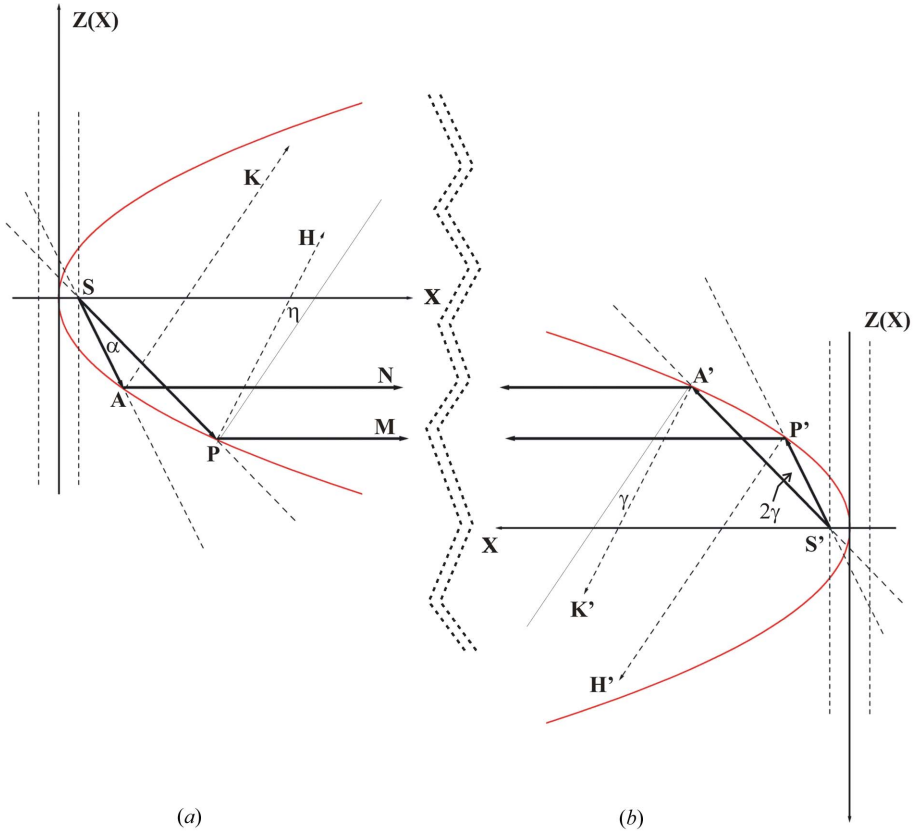


**Figure 2**
Ray paths in parabolic collimating (*a*) and refocusing (*b*) mirrors.

The second option in (4*a*) also describes the case of a beam size on the first mirror that is intentionally limited by a slit preceding the mirror (mirror mapping).

The quantities $\alpha'_{\rm c}$ and $\Delta'_{\rm s}$ act as *collimator-like* terms, which mimic the finite planar angular acceptance of the first mirror ($\alpha'_{\rm c}$) and the sample or a slit before it ($\Delta'_{\rm s}$) owing to their finite dimensions. Since the beam is almost parallel between the collimating and the refocusing mirror, and because the mirrors are assumed to have almost equal dimensions, no further collimating term is considered before the second mirror.

With respect to Sabine's expression (1), equation (3) includes two additional probabilities due to the presence of the collimating and the refocusing mirrors, and two additional integrals over the angles $\eta$ and $\gamma$, which describe the local angular tilt, with respect to a reference direction, of the normal to the first and the second mirror surfaces. Let us consider the collimating mirror described in Fig. 2(*a*). The path of the

central (reference) ray that is reflected by the mirror surface at its pole $P$ is $SPM$, and $SAN$ is the path of an individual ray with divergence $\alpha$ with respect to the centerline and which is reflected by the mirror at $A$. $PH = n_P$ and $AK = n_A$ are the normals to the mirror surface at $P$ and $A$. For a perfectly collimating mirror, the angular tilt $\eta$ of the normal to the mirror surface between $P$ and $A$ is given by the angle between the normals $n_P$ and $n_A$: $\eta = \alpha/2$. Therefore, the quantity $(2\eta - \alpha)$ expresses the residual divergence out of the collimating mirror of the individual ray $AN$ with respect to the centerline $PM$, and its integral over all mirror surface points will be zero only in the case of a perfectly collimating mirror. Analogously (see Fig. 2*b*), $2\gamma$ expresses the divergence out of the refocusing mirror of the individual ray $A'S'$ with respect to the centerline $P'S'$, and its integral over all mirror surface points will be equal to the source divergence $\alpha_m$ only in the case of a perfectly refocusing mirror and no limiting slits in between. We observe that the integration in $\eta$ and $\gamma$ in equation (3) is equivalent to adopting a statistical approach to the problem of estimating the IRFs in the presence of collimating and focusing optics. The real value of the normal to the surface at each point of the mirror is, therefore, not accessible as it is with ray-tracing approaches. At each point of the mirror, an average over all possible values of the surface normal that lead to a non-zero reflection probability (*i.e.* within the width of the divergence distributions) is, instead, calculated. It should be noted that the sketches in Fig. 2 simply explain the meaning of the equation (3) variables without reflecting the adopted statistical approach.

Equation (3) is general and can be written for both ideal and real mirrors and for all mirror settings, *e.g.* first and second mirror flat (flat–flat), first and second mirror bent (bent–bent), and first mirror bent and second mirror flat (bent–flat). The ideal bent–flat and flat–flat would, then, be obtained by setting $\gamma$ (bent–flat) or both $\gamma$ and $\eta$ (flat–flat) to zero and sending $\Delta\tau'_f$ (bent–flat) or both $\Delta\tau'_p$ and $\Delta\tau'_f$ (flat–flat) to infinity before integrating equation (3) in $d\alpha$ and $d\delta$.[3] The result of the integration would be Sabine's expression (2).

The integration of equation (3) gives a simple analytical expression:

$$\Delta^2(2\theta) = \left(\Delta\tau_p^2 + \Delta_m^2/2\right)\left(\tan\theta_a/\tan\theta_m - 2\tan\theta/\tan\theta_m\right)^2 + \Delta_a^2 + \Delta\tau_{f,\mathrm{effective}}^2. \quad (5)$$

Note that when dealing with real collimating and refocusing mirrors that never produce a beam of perfectly zero or $\alpha_m$ divergence, expression (5) is always applicable and eventually allows one to diagnose incorrect settings of the mirror radii of curvature, as explained in §4. For a given optical system, equation (5) can be directly employed to fit the experimental data with $\Delta\tau_p$ and $\Delta\tau_f$ as fitting parameters.

[3] We observe that flattening the collimating mirror translates into a fairly poor energy resolution (beam of divergence $\alpha_m$ directly impinging on the first monochromator crystal). Therefore, the flat–flat optical configuration is not recommended for high-resolution powder diffraction studies, unless the intrinsic divergence of the source is very small as in the case of undulators (Gozzo *et al.*, 2004).

We observe that often a slit before the first mirror is used in order to collimate further the beam emitted by the source (as is the case at the SLS-MS beamline). In this case, the higher the angle of incidence on the mirror, the higher its angular acceptance. Translated into photon energies, this means that the lower the energy, the higher is the collection by the mirror of secondary diffraction maxima produced by the slit preceding the first mirror. We expect, therefore, that for low-energy photons, the model becomes less predictive since the source probability function would be less suitably described by a Gaussian function.

## 4. Beam divergence contribution terms in the presence of mirrors

Details of the theoretical derivation of the divergence distribution widths $\Delta\tau'_p$ and $\Delta\tau'_{f,\mathrm{effective}}$ are available as supplementary information. We describe here only the principle of this derivation and define the bending parameters $c_i$ for the collimating ($i = 1$) and refocusing ($i = 2$) mirrors that we employ in the discussion of the simulation and the modeling of the instrumental resolution functions performed in §§6 and 7. Using the Lioville theorem, we also derive the collimator-like terms $\Delta'_s$ and $\alpha'_c$, already introduced in §3, for an optical system such as that described in Fig. 1.

Analytical expressions of an ideal parabolic mirror profile and of real collimating or refocusing mirror profiles are determined (see mathematical details in the supplementary information), which take into account the mirror symmetric bending approximation and gravity and thermal deformation effects. The FWHM of the beam angular divergence $\Delta\tau_p$ and $\Delta\tau_f$ can then be derived as maximum angular deviations from the ideal values of the normal to the mirror surfaces. For both mirrors a numerical bending coefficient $c_i$ is defined, providing an indication of the departure of the real mirror from the ideal one (see mathematical details in the supplementary information). For the first collimating mirror at the SLS-MS beamline, the optimum $c_1$ value, which is a function of the photon energy, is 0.8, 0.73 and 0.5 for 10, 13 and 25 keV, respectively. The corresponding $\Delta\tau_p$ value is then 15 µrad. Analogously, for the SLS-MS beamline refocusing mirror in bent–bent configuration, the bending parameter $c_2$ should ideally be equal to 1 for all energies, with $c_2 > 1$ ($< 1$) indicating overbending (underbending), whereas the ideal $c_2$ value in a flat configuration should, for all energies, be 0.25.

Analytical expressions for equations (4*a*) and (4*b*) in §3 (given already as FWHM values) can be determined making use of Liouville's theorem (Arndt, 1990). Let us consider a simple optical configuration consisting of a source and a collimating mirror (such as the first mirror in Fig. 1). Defining $f$ as the source size, $\alpha_c$ as the planar angle of collection of rays from the source by the mirror, $w$ as the beam width after reflection by the mirror and $\Delta\varphi$ as its divergence (also called the crossfire of the beam), the theorem can be expressed as $f\alpha_c = w\Delta\varphi$. For a point-like source and a finite $\alpha_c$, $\Delta\varphi$ would obviously be equal to zero and $w$ would be given by $L_1\sin\theta_1$, with $L_1$ the length of the mirror and $\theta_1$ the mirror grazing

incident angle. According to Liouville's theorem, the larger the size $f$ of the source, the larger the divergence $\Delta\varphi$ of the outgoing beam. The divergence $\Delta\varphi$ will then be given by $\Delta\varphi = w/d$, where $d$ is the distance between the mirror and the virtual focus situated behind the mirror for a divergent beam and before it for a convergent beam. For a parallel beam $d \rightarrow \infty$. If the beam of width $w$ and divergence $\Delta\varphi$ is reflected by a second flat mirror (length $L_2 \simeq L_1$ and incident angle $\theta_2 \simeq \theta_1$) and a sample of size $s$ is placed along the beam path, the divergence of the beam at the sample position will still be $\Delta\varphi$ only if $s \geq w$. In this case, according to (4*a*), $\Delta\tau_{\rm f,effective} = \Delta\tau_{\rm f} \simeq \Delta\varphi$. If $s < w$, we would, instead, have $\Delta_{\rm s} \cong s/d = s/w\Delta\varphi \cong s/(L_2 \sin\theta_2)\Delta\varphi$ and $\Delta\tau_{\rm f,effective} = \Delta_{\rm s}$. If the second mirror is a refocusing mirror, the spot size will obviously be much smaller, and if $s \geq w$, as is often the case in powder measurements, then $\Delta\tau_{\rm f,effective} = \Delta\tau_{\rm f} \simeq L_2 \sin\theta_2/p_2 \simeq L_1 \sin\theta_1/p_1 \simeq \alpha_{\rm c}$. If, in spite of the second mirror, the size of the sample (or the width of the slit before it) $s$ is still smaller than the spot size at the sample position then $\Delta\tau_{\rm f,effective} = \Delta_{\rm s} \cong s/(d - p_2) \cong s/p_2$. Thus, for the optical system described in Fig. 1, we can summarize

$$\text{sample size} < \text{spot size} \rightarrow \Delta\tau_{\rm f,effective} = \Delta_{\rm s} \cong \begin{cases} \text{Bent} - \text{flat} \rightarrow s/(L_2 \sin\theta_2)\Delta\varphi \simeq s/(L_2 \sin\theta_2)\Delta\tau_{\rm p} \\ \text{Bent} - \text{bent} \rightarrow s/p_2 \end{cases} \quad (6)$$

$$\text{sample size} \geq \text{spot size} \rightarrow \Delta\tau_{\rm f,effective} = \Delta\tau_{\rm f} \cong \begin{cases} \text{Bent} - \text{flat} \rightarrow \Delta\varphi \simeq \Delta\tau_{\rm p} \\ \text{Bent} - \text{bent} \rightarrow L_2 \sin\theta_2/p_2 \simeq L_1 \sin\theta_1/p_1 \simeq \alpha_{\rm c}. \end{cases} \quad (7)$$

Using similar arguments, we find that $\alpha_{\rm c} \simeq L_1 \sin\theta_1/p_1$ and $\alpha_{\rm m,effective} = \alpha_{\rm c}$ whenever the finite angular acceptance of the collimating mirror limits the natural divergence of the source $\alpha_{\rm m,effective}$.

## 5. Additional contributions to the IRF

In order approximately to take small isotropic sample effects into account in our equation (5), we considered the classical Scherrer (1918) equation for the size and the Bragg law differentiation for the strain as additional terms to be added quadratically to the IRF:

$$\text{FWHM}(2\theta)^2 = \Delta(2\theta)^2 + \Delta(2\theta)^2_{\text{sample grain size}} + \Delta(2\theta)^2_{\text{strain}}. \quad (8)$$

In addition to the sample grain size and strain contributions, mirror manufacturing slope errors could modify the ideal parabolic mirror profiles. The expressions $\Delta\tau_{\rm p}$ and $\Delta\tau_{\rm f,effective}$ describing the FWHM of the angular distribution of the beam after reflection onto the first and second mirrors would then have a more general expression:

$$\Delta\tau_{\rm p}^2 \rightarrow \Delta\tau_{\rm p}^2 + \Delta_{\rm se-1}^2, \qquad \Delta\tau_{\rm f,effective}^2 \rightarrow \Delta\tau_{\rm f,effective}^2 + \Delta_{\rm se-2}^2, \quad (9)$$

where the terms $\Delta_{\rm se-\mathit{i}}^2$ take into account the mirror manufacturing slope errors for the first and the second mirror, respectively. Usually a good estimate of this contribution should be provided by the mirror's manufacturing company (typically of the order of few microradians).

Note that in the bent–bent case, the correction (9) is negligible since $\Delta\tau_{\rm f,effective}^2$ is, in this case, of the order of the source angular divergence.

## 6. Theoretical simulations and discussion

Computations using equation (5) were performed at three photon energies (10, 13 and 25 keV) using the SLS Materials Science beamline powder station experimental parameters (Patterson *et al.*, 2005). Fig. 3 shows the prediction of our model when the theoretical values for the mirror angular divergences obtained in §3, for $c_1 = c_{1,\rm optimum}$ and $c_2 = c_{2,\rm optimum}$

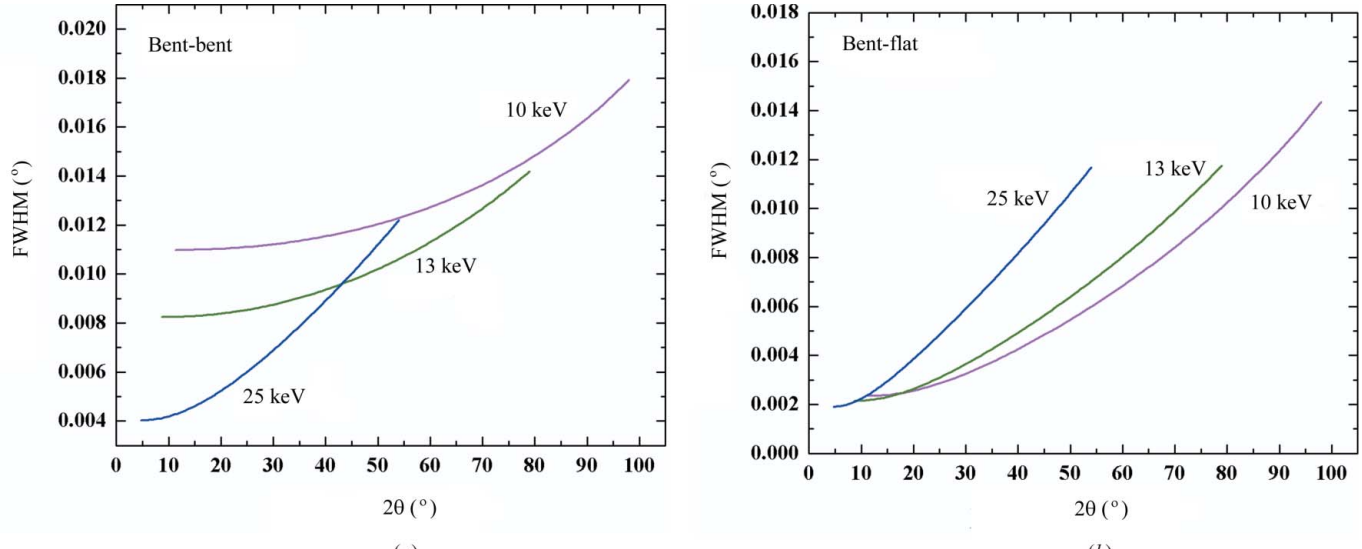


(*a*) (*b*)

**Figure 3**
Computation of the IRF for $c_1 = c_{1,\rm optimum}$ (equal to 0.8, 0.73 and 0.5 for 10, 13 and 25 keV) and $c_2 = c_{2,\rm optimum} \cong 1$ in the bent–bent case (*a*), and for $c_1 = c_{1,\rm optimum}$, $c_2 = 0.25$ in the bent–flat case (*b*) at 10, 13 and 25 keV, assuming that both sample and thermal expansion effects are negligible.

in the bent–bent case (Fig. 3*a*) and for $c_1 = c_{1,\mathrm{optimum}}$, $c_2 = 0.25$ in the bent–flat case (Fig. 3*b*), are employed in equation (5). Sample grain size and thermal deformation corrections were neglected. Note that the IRF curves at different photon energies have, in the bent–flat case, an opposite dependence on the energy with respect to the bent–bent case.

Small sample grain size and strain contributions, approximately taken into account using the correction (8), can be appreciated in Fig. 4 at 13 keV. An average linear size $D$ of the powder crystallites of 2 µm (dashed curves) and a strain contribution of $5 \times 10^{-5}$ (dashed–dotted curves) have been simulated, and the continuous curves are the theoretical simulations of Fig. 3 included for reference. The size leads to a shift of the curve towards higher FWHMs, whereas the strain influences the curve's slope.

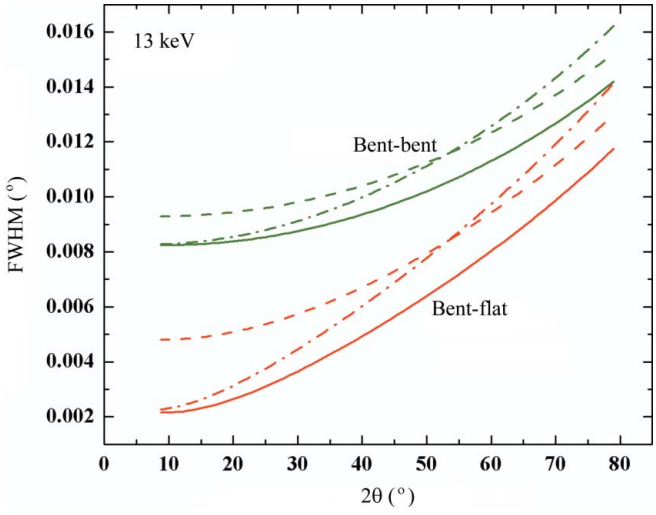


**Figure 4**
Computed size ($D$ = 2 µm, dashed curves) and strain ($5 \times 10^{-5}$, dashed–dotted curves) effects for the bent–bent and bent–flat cases at 13 keV. The continuous curves are the computations of Fig. 3, included for reference.

For the three photon energies, Fig. 5 simulates IRF curves in the bent–flat case with a size effect of $D$ = 2 µm. Note that a grain size of only 2 µm eliminates the overlapping of the curves at low $2\theta$ values and reverses the dependence as a function of the energy.

Fig. 6 shows the effects of different bendings on the IRF FWHMs. In particular, we have plotted the theoretical simulations of the IRF at 13 keV in the bent–bent case for ($c_1$, $c_2$) = (1, 1) (continuous black curve), ($c_1$, $c_2$) = (0.75, 1) (dashed green curve), ($c_1$, $c_2$) = (1.25, 1) (dashed–dotted green curve), ($c_1$, $c_2$) = (1, 0.75) (dashed red curve) and ($c_1$, $c_2$) = (1, 1.25) (dashed–dotted red curve), assuming that both sample grain size and thermal deformation effects are negligible. We observe that an underbending (overbending) of the first collimating mirror with respect to $c_1$ = 1 decreases (increases) the IRF curvature, thus causing the FWHM values to become smaller (larger) at large $2\theta$ angles. On the other hand, an underbending (overbending) of the second refocusing mirror with respect to $c_2$ = 1 almost rigidly shifts the IRFs downwards (upwards). The effect of lowering the FWHM values at larger $2\theta$ angles when decreasing $c_1$ below 1 only occurs until the optimal underbending of the first mirror is reached (corresponding to $c_1 = c_{1,\mathrm{optimum}}$), which compensates as much as possible for gravity and aberrations. Further lowering $c_1$ below this optimal values causes an increment of the IRF FWHM of up to 4% of its value at $c_1 = c_{1,\mathrm{optimum}}$.

## 7. Experimental tests

### 7.1. Beamline and diffractometer optics

All experimental data presented here were collected at the SLS-MS beamline powder diffraction station described in Fig. 1. This station is situated 36 m from the source and is one

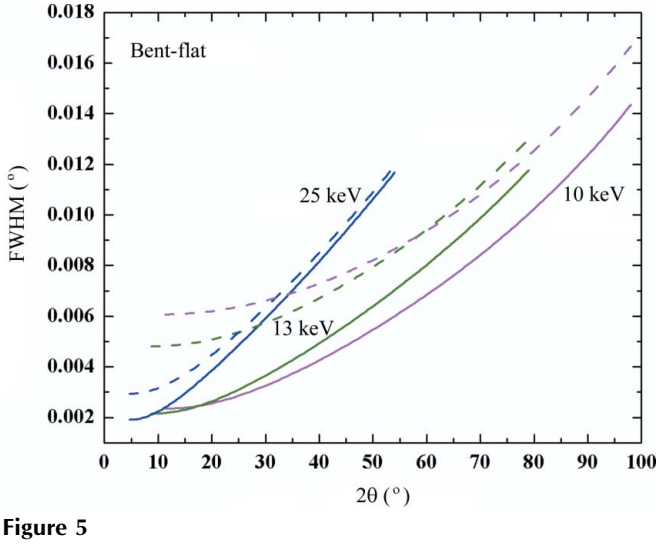


**Figure 5**
Computed size effect ($D$ = 2 µm, dashed curves) at 10, 13 and 25 keV for the bent–flat case, compared with the computations (continuous curves) of Fig. 3.

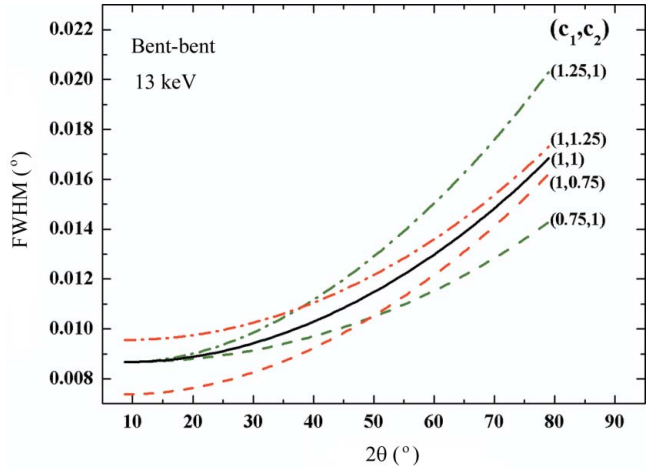


**Figure 6**
Computations at 13 keV in the bent–bent case for ($c_1$, $c_2$) = (1, 1) (continuous black curve), ($c_1$, $c_2$) = (0.75, 1) (dashed green curve), ($c_1$, $c_2$) = (1.25, 1) (dashed–dotted green curve), ($c_1$, $c_2$) = (1, 0.75) (dashed red curve) and ($c_1$, $c_2$) = (1, 1.25) (dashed–dotted red curve), assuming that both sample and thermal deformation effects are negligible.

of the three stations served by the beamline optics (Patterson *et al.*, 2005). The other two stations are the tomographic microscopy (Stampanoni *et al.*, 2002) and the surface diffraction (Willmott *et al.*, 2005) stations at 31 and 41 m from the source.

The powder diffractometer is a two-plus-one axis diffractometer; an $\omega$ axis hosts the sample and two $2\theta$ axes host two independent detection systems, *viz.* a multicrystal analyzer detector for high angular resolution measurements and a fast-read-out solid-state microstrip detector that collects 60° in $2\theta$ at once as described by Schmitt *et al.* (2004, and references therein). In the present article, we only discuss the powder diffractometer in relation to its high-resolution setting (Cernik *et al.*, 1990; Fitch, 2004; Gozzo *et al.*, 2004; Knapp *et al.*, 2004; Toraya *et al.*, 1996). The multicrystal analyzer detector consists of five Si(111) crystals mounted at a nominal angular offset of 2° on a $\theta_a$–$2\theta_a$ two-circle goniometer. The $\theta_a$-axis goniometer plate positions the five crystals at the correct Bragg angle for a given photon energy, while the $2\theta_a$-axis goniometer plate positions, as a unit, the corresponding five NaI(Ti) scintillator/photomultiplier detectors at the right $2\theta_a$ value for the selected photon energy (Hodeau *et al.*, 1998). Diffraction patterns are collected either in step-by-step or on-the-fly mode. The former positions the $2\theta$ arm motor at each $2\theta$ step, whereas the latter continuously runs the $2\theta$ arm while the intensity signal is read at variable frequency (up to 50 Hz). Data from the five analyzer crystals are then rebinned at the appropriate $\Delta 2\theta$ step size and merged after carefully correcting the crystal offsets. Full-pattern acquisition times typically range from 15 min to several hours depending on the selected photon energy, mirror setting, sample scattering powder and requested counting statistics.

### 7.2. Line broadening reference sample

Full diffraction patterns were collected at three different photon energies (10, 13 and 25 keV) using the fluoride $Na_2Ca_3Al_2F_{14}$ (Courbion & Ferey, 1988), denoted NAC hereafter, and the Si(111) multicrystal analyzer detector. To our knowledge, NAC is the sample with the smallest intrinsic line width presently available and, therefore, the most appropriate for studying the instrumental contribution to the diffraction peak broadening, in particular in the case of high-resolution instruments. However, NAC is not available as a NIST standard reference material and, therefore, there are no certified values for lattice parameters, average grain size and residual strain. The NAC lattice parameters and structure were taken from the literature (Courbion & Ferey, 1988).

### 7.3. Data acquisition details

The NAC powder was mounted in 0.5 mm Lindemann capillaries and the capillaries were spun at approximately 5 Hz. During the beamline optical setup, the rocking curve of the second monochromator crystal and the crystal analyzer rocking curve in the attenuated (1, −1, 1, −1, −1) configuration (no sample) were collected as part of a routine procedure that we perform to adjust the compensation to the monochromator thermal load (mono-RC) and the beam profile (analyzer-RC), which varies over a wide range depending on the refocusing mirror curvature setting. The zero offset of the $2\theta$ scale was also adjusted under the same conditions of the analyzer-RC collection. The analyzer-RCs, reflecting the pure angle-independent instrumental profile (Masson *et al.*, 2003), are at the SLS-MS beamline typically Gaussian curves, like that shown in Fig. 7 corresponding to the 13 keV bent–bent configuration. However, a poor compensation of the thermal load can produce longer tails in the mono-RC, whereas a substantial focusing or an over-focusing of the second mirror often introduces aberration in the analyzer-RC. The small shoulder that appears to be present on the left-hand side of Fig. 7 disappears when the second mirror bending is relaxed, but it can also become more severe under different focusing conditions and/or at different energies. We note that 'super-Lorentzian' profiles were observed by Masson *et al.* (2003) at the BM16 powder diffraction at the European Synchrotron Radiation Facility (ESRF) in Ge(111) analyzer rocking curves; the authors attributed these profiles to the presence of surface defects and strain or to low-angle asymmetry of the Si(111) analyzer profile, which was attributed by the same authors to curvature effects during the crystal mounting procedure. Such profiles were never observed at the SLS-MS beamline powder station, making the Gaussian approximation of our model reasonably applicable to the experimental data collected at this station. The beam size on the sample was shaped using a set of slits mounted very close to the sample and its value was kept at approximately 0.45 (vertical) × 5.5 (horizontal) mm for all photon energies. The beam size at the sample was measured using a home-made X-ray eye (XRE) imaged onto a CCD camera. For all photon energies, full diffraction patterns of NAC were collected in bent–bent and bent–flat optical configurations and on-the-fly data acquisition mode, observing an intensity reduction of approximately one order of magnitude when flattening the

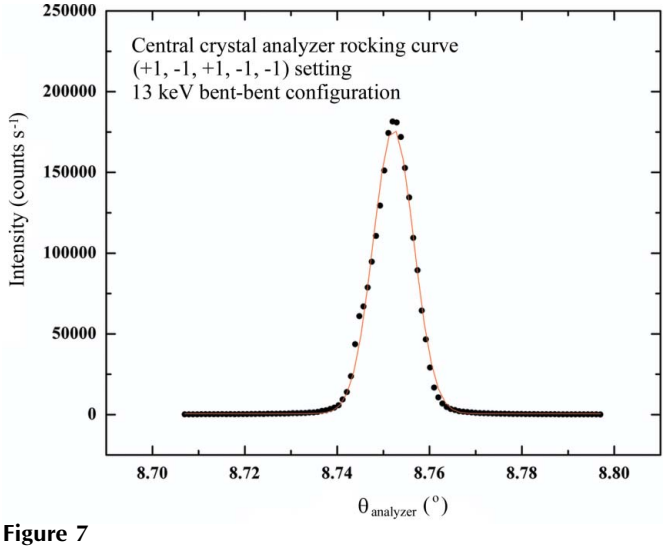


**Figure 7**
Si(111) analyzer rocking curve in the dispersive (1, −1, 1, −1, −1) setting collected at 13 keV in the bent–bent configuration. The experimental points (dots) were fitted to a pure Gaussian profile (line).

refocusing mirror. The beam intensity (photons per second) variation at the SLS-MS beamline as a function of the photon energy is described in detail by Patterson *et al.* (2005). Data were rebinned at $\Delta 2\theta = 0.0008^\circ$ for all energies using only the signal from the central crystal, except at 25 keV for which the signal from the three central crystals was merged to improve the counting statistics. Acquisition times ranged between 3 and 6 h. The full diffraction patterns in bent–bent and bent–flat configurations were collected keeping all beamline and diffractometer optical elements, other than the second mirror, strictly identical. Moving from the bent–bent to the bent–flat optical configuration only required a slight correction of the $2\theta$ zero value.

### 7.4. Data analysis strategy and experimental results

In order to verify experimentally the validity of equation (5), a number of isolated peaks (around 15) were selected from all experimental full patterns to perform a single-peak least-squares fit and determine their FWHMs. In spite of the Gaussian character of the instrumental profile, the line shape of the NAC diffracted peaks was well described by a pseudo-Voigt profile convoluted with the Finger–Cox–Jephcoat (FCJ) asymmetric function (Finger *et al.*, 1994) to correct the low-angle peak asymmetry due to axial divergence. For each peak, a linear background was adopted, and the coefficients were refined together with the FWHM, the Gaussian and the Lorentzian fractions of the pseudo-Voigt profile shape function, and the peak position. The FCJ function's parameters were measured experimentally; their values were only slightly refined around the initial values for the lowest $2\theta$-angle peaks and were then kept fixed during the single-peak refinement. The single-peak fits were performed using routines from the *Quanto* program (Altomare *et al.*, 2001), suitably modified to execute Finger's (1998) routines, implementing the FCJ algorithm discussed above. The values found for the mixing parameter $\eta$ were approximately 0.35 (0.45), 0.4 (0.5) and 0.25 (0.35) for the bent (flat) refocusing mirror at 10, 13 and 25 keV, respectively.

The experimental FWHMs were compared with equation (5) predictions starting first with theoretical $\Delta_a$, $\Delta_m$, $\Delta\tau_p$ and $\Delta\tau_{f,\mathrm{effective}}$ values and then trying to adjust the $\Delta\tau_p$ and $\Delta\tau_{f,\mathrm{effective}}$ parameters (or equivalently $c_1$ and $c_2$) within reasonable values. A slope error contribution of 2 µrad, as quoted by the mirror manufacturing company, was also taken into account. The comparison clearly confirmed the presence of a non-negligible size effect already qualitatively observed when comparing the pure instrumental and the sample powder profiles. Equation (5) was then corrected as in equation (8) to include an approximate size effect, and all curves were fitted simultaneously to determine the best estimates of $\Delta\tau_p$ and $\Delta\tau_{f,\mathrm{effective}}$ under this hypothesis. An estimate of 1.45 µm grain size simultaneously satisfied all six data sets.

In order to check the robustness of our results against the crude Gaussian approximation for the small, but still not negligible, sample size contribution [equation (8)] and the correlation between mirror bending and sample size effects on the peak broadening (see §6), we also addressed the problem within a full-pattern Rietveld refinement approach (Rietveld, 1969). All NAC diffraction patterns were least-squares fitted using the *FullProf* program (Rodriguez-Carvajal, 1993) and a modified pseudo-Voigt profile (Thompson *et al.*, 1987) convoluted with the FCJ asymmetry function, according to the previous single-peak fit indications. Since the *U*, *V* and *W* parameters of the modified pseudo-Voigt implemented in *FullProf* reflect the pure Gaussian contribution to the peak profile, whereas the *X* and *Y* parameters reflect the pure Lorentzian contribution to the peak profile, under the assumption that the sample intrinsic effects are only represented by a Lorentzian contribution (not strictly correct), *U*, *V* and *W* parameters were derived according to equation (5) using the $\Delta\tau_p$ and $\Delta\tau_{f,\mathrm{effective}}$ values from the previous fit. These were then fixed (or slightly refined) during the *FullProf* refinements, while the *X* and *Y* parameters were left free to vary. A summary of the full-pattern *FullProf* fitting parameter values has been deposited as supplementary information. The $2\theta$ zero and the background were also refined, the latter starting from a user-supplied table of background points. The goodness-of-fit (GoF) indicator (McCusker *et al.*, 1999, equation 12) of the fits ranged from 1.3 to 1.6, except for the 13 keV data in the bent–bent configuration, for which it was 2.7. We observe that the FWHM values of the single-peak approach were found to be in good agreement with the *FullProf* results. Fig. 8 shows, as an example, the comparison between the full-pattern refinement fits (*FullProf*, circles) and the single-peak fits (modified-*Quanto*, stars) in the case of 13 keV.

Using the Lorentzian component of the profile widths, as given by the *FullProf* program, Williamson–Hall plots, like that shown in Fig. 9, were constructed with data at 10 and 13 keV in the bent–flat optical configuration. Data at 25 keV were excluded because they resulted from the merging of three analyzer crystals. The estimated size effect using the two

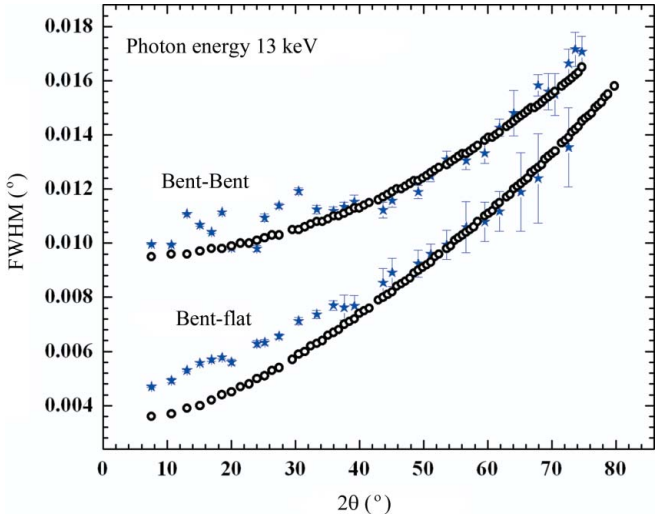


**Figure 8**
Comparison at 13 keV of the FWHM values obtained as a result of the full-pattern *FullProf* refinement fits (circles) and single-peak *Quanto* refinement fits (stars).

**Table 1**
Results of the fits of the experimental peak widths *versus* $2\theta$ curves at 10, 13 and 25 keV to equation (5) corrected as in equation (8) to include a size effect of 2.0 µm.

The theoretical values are also reported for comparison. For the bent–flat configuration the residual divergence of 23 µrad corresponding to $c_2 = c_{2,\text{optimum}} = 0.25$ was found to be compatible with all experimental data without introducing any fitting parameter, as discussed in the text.

| Photon energy (keV) | $\alpha_m$ (mrad) | $\alpha_{m,\text{effective}}$ (mrad) | $\Delta\tau_p^{\text{theor}}$ (µrad) at $c_{1,\text{opt}}$<br>$\Delta\tau_p^{\text{fit}}$ (µrad)<br>($c_1^{\text{theor}}$; $c_1^{\text{fit}}$)<br>1st mirror bent | $\Delta\tau_{f,\text{effective}}^{\text{theor}}$ (mrad) at $c_{2,\text{opt}}$<br>$\Delta\tau_{f,\text{effective}}^{\text{fit}}$ (mrad)<br>($c_2^{\text{theor}}$; $c_2^{\text{fit}}$)<br>2nd mirror bent | $\Delta\tau_{f,\text{effective}}$ (µrad)<br>2nd mirror flat |
|---|---|---|---|---|---|
| 10 | 0.23† | 0.18 | 15<br>$51 \pm 10$<br>(0.80; 1.60) | 0.18<br>$0.24 \pm 0.02$<br>(1; 1.31) | ≤ 23‡ |
| 13 | 0.214 | 0.15 | 15<br>$22 \pm 5$<br>(0.73; 0.98) | 0.14<br>$0.15 \pm 0.01$<br>(1; 0.92) | ≤ 23 |
| 25 | 0.154 | 0.08 | 15<br>$20 \pm 2$<br>(0.50; 0.87) | 0.07<br>$0.15 \pm 0.01$<br>(1; 0.72) | ≤ 23 |

† Limited by a diaphragm. ‡ Values of residual divergences smaller than 23 µrad leave the curves unchanged.

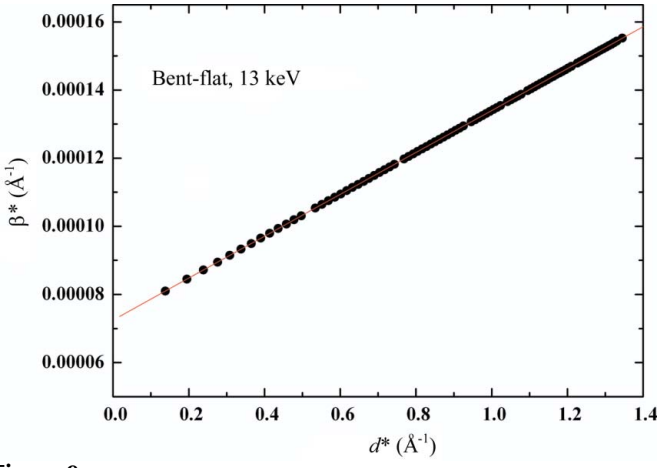


**Figure 9**
Williamson–Hall plot built using the Lorentzian integral breaths as extracted from the full-pattern *FullProf* fits for 13 keV in bent–flat configuration.

data sets was fairly consistent (1.3 µm at 13 keV and 1.5 µm at 10 keV) and a negligible strain effect was found in both cases.

As a final check, the *FullProf* FWHMs were then modeled to equation (8). A particle size of 2.0 µm was necessary to adjust the experimental FWHMs to the model with $\Delta\tau_p$ and $\Delta\tau_{f,\text{effective}}$ values acceptable and close to the values previously estimated with the single-peak fits. Figs. 10 and 11 show the experimental curves (dots) and their fits to equation (8) (lines) for 10, 13 and 25 keV photon energies in the bent–bent and bent–flat optical configurations. In spite of the crude approximation of a pure Gaussian-like size effect, which the profiles clearly show to be of Lorentzian character, the agreement between the experimental data and the model is reasonably good. Comparing all FWHM *versus* $2\theta$ plots in a $\delta q$ (Å$^{-1}$) *versus* $q^{-1}$ plot, we found that at a given photon energy the bent–flat configurations are, as expected, the most resolved ones and that 13 keV corresponds to the highest angular resolution ranging from 0.000075 to 0.00018 Å$^{-1}$.

Table 1 reports the results of the fits and their comparison with the expected values. The values found for the bending parameters $c_1$ and $c_2$ show that the first mirror was slightly overbent for 13 keV, whereas a more significant overbending was detected for both 10 and 25 keV, the former being more severe. In the bent–bent case, the $c_2$ value was very close to $c_{2,\text{optimum}}$ ($\simeq 1$) for 13 keV but larger for 10 keV and smaller for 25 keV, indicating overbending and underbending, respectively. For the bent–flat configuration we found that the residual divergence of 23 µrad [$c_2 = c_{2,\text{optimum}}$ ($\simeq 0.25$)], entirely due to the fourth-order uncompensated gravity sag and slope errors, is compatible with all experimental data without

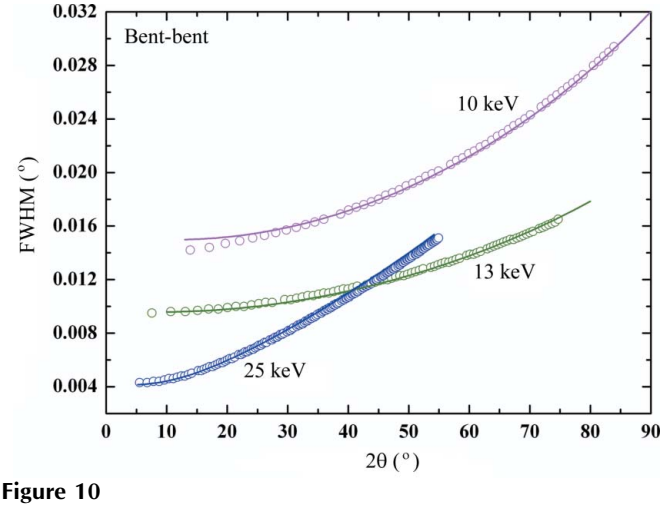


**Figure 10**
Experimental IRFs (circles) and their fit to equation (8) to include a size effect of 2.0 µm (lines) and negligible strain for 10, 13 and 25 keV photon energies in the bent–bent optical configuration.

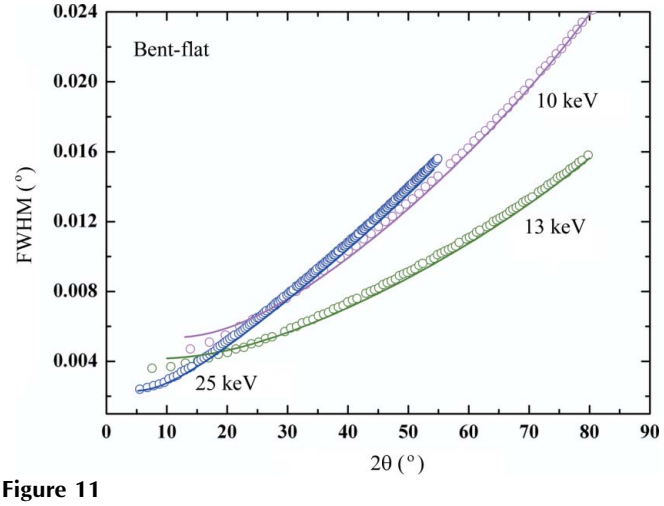


**Figure 11**
Experimental IRFs (dots) and their fit to equation (8) to include a size effect of 2.0 µm (lines) and negligible strain for 10, 13 and 25 keV photon energies in the bent–flat optical configuration.

the need to introduce any fitting parameter. Looking at Table 1, we observe that in the bent–bent configuration $\Delta\tau_{\rm f,effective} \simeq \alpha_{\rm m,effective}$ for both 13 and 25 keV, which is what we expect since the optics at the SLS Materials Science beamline are one-to-one (magnification equal to one), but at 10 keV we have $\Delta\tau_{\rm f,effective} \neq \alpha_{\rm m,effective}$. We believe that this effect is due to the fact that, at low energies, the angular acceptance of the first mirror $L_1 \sin\theta_1/p_1$ (0.28 mrad at 10 keV) is larger than $\alpha_{\rm m}$. Thus, at 10 keV, secondary diffraction maxima are collected by the first mirror, and the source would then be less suitably described by a Gaussian function. On the other hand, at 13 keV, $L_1 \sin\theta_1/p_1 \cong \alpha_{\rm m}$, and at 25 keV, $L_1 \sin\theta_1/p_1 < \alpha_{\rm m}$.

## 8. Concluding remarks

Our model offers a simple analytical approach to tackling the problem of predicting the IRF behavior for synchrotron radiation powder diffractometers with focusing optics. Since our model is based on the Gaussian approximation, it requires that the character of the instrumental broadening be mostly Gaussian, as can be verified through the analysis of the analyzer rocking-curve shape in the (1, −1, 1, −1, −1) setting as suggested by Masson *et al.* (2003). Our experimental data demonstrate that, with a careful beamline optical setup and in the absence of systematic aberration effects, which are typically due to analyzer surface defects, strain and curvature effects induced during the mounting of crystals, this is, indeed, possible. High-resolution powder diffraction experiments for microstructural analyses should, therefore, be performed, at the SLS-MS beamline, under these experimental conditions.

With a Gaussian beamline optical setup, the availability of a standard with negligible or at least small and well characterized intrinsic contributions to the peak profile would allow a straightforward application of our model to determine the pure instrumental resolution function of a synchrotron-radiation-based powder diffractometer with focusing optics. Equation (5) could then be plausibly implemented in a Rietveld refinement program.

The large discrepancy between the accurate NAC grain size estimate of 3.6 μm by Masson *et al.* (2003) and our rough estimate of 1.3–1.5 μm is above the inaccuracy expected from correcting, as we did, equation (5) with a Gaussian term to include the size effect, and seems, therefore, to indicate that NAC is probably not always available with identical intrinsic characteristics. We therefore plan to perform additional measurements on several other standards with certified size and strain characteristics.

We dedicate this article to the memory of some very special people, Anna and Lidia Cortese, Elio Rizzo, Anna and Dante Giannini, and Antonio De Caro. We thank Bruce Patterson for his precious advice on the beamline optics and for fruitful discussions during several phases of the development of this work, David Maden for his excellent work in computer controlling the beamline and the powder station, and Michael Lange and Dominik Meister for their competent technical assistance at the beamline. We also thank Anna Bianco for kindly sharing some of her deep knowledge on synchrotron radiation optics with us, and Aziz Daouid Aladin who made our debut in the complex world of *FullProf* much easier and helped us to discover some of the powerful capabilities of this wonderful program during informal friendly *fitting-dinners*. Finally we thank our kids, Antonella, Dominique, Justine, Julie, Matthieu and Pietro, for being so often so patient with us.

## References

Altomare, A., Burla, M. C., Giacovazzo, C., Guagliardi, A., Moliterni, A. G. G., Polidori, G. & Rizzi, R. J. (2001). *J. Appl. Cryst.* **34**, 392–397.
Arndt, U. W. (1990). *J. Appl. Cryst.* **23**, 161–168.
Balzar, D., Stephens, P. W. & Ledbetter, H. (1997). *Fiz. A*, **6**, 41–50.
Caglioti, G., Paoletti, A. & Ricci, F. P. (1958). *Nucl. Instrum.* **3**, 223–228.
Caglioti, G., Paoletti, A. & Ricci, F. P. (1960). *Nucl. Instrum. Methods*, **9**, 195–198.
Caglioti, G. & Ricci, F. P. (1962). *Nucl. Instrum. Methods*, **15**, 155–163.
Cernik, R. J., Murray, P. K. & Pattison, P. (1990). *J. Appl. Cryst.* **23**, 292–296.
Courbion, G. & Ferey, G. (1988). *J. Solid State Chem.* **76**, 426–431.
Cox, D. E. (1991). *Handbook on Synchrotron Radiation*, Vol. 3, pp. 157–200. Amsterdam: North-Holland.
Cox, D. E., Toby, B. H. & Edy, M. M. (1988). *Aust. J. Phys.* **41**, 117–131.
Finger, L. W. (1998). *J. Appl. Cryst.* **31**, 111.
Finger, L. W., Cox, D. E. & Jephcoat, A. P. (1994). *J. Appl. Cryst.* **27**, 892–900.
Fitch, A. N. (2004). *J. Res. Natl Inst. Stand. Technol.* **109**, 133–142.
Gozzo, F., Schmitt, B., Bortolamedi, Th., Giannini, C., Guagliardi, A., Lange, M., Meister, D., Maden, D., Willmott, P. & Patterson, B. D. (2004). *J. Alloys Compd*, **362**, 206–217.
Hastings, J. B., Thomlinson, W. & Cox, D. E. (1984). *J. Appl. Cryst.* **17**, 85–95.
Hodeau, J.-L., Bordet, P., Anne, M., Prat, A., Fitch, A. N., Dooryhee, E., Vaughan, G. & Freund, A. K. (1998). *Proc. SPIE*, **3448**, 353–361.
Howells, M. R. (1994). *New Directions in Research in Third-Generation Soft X-ray Synchrotron Radiation Sources*, edited by A. S. Schlachter & F. J. Wuilleumier, pp. 359–385. Dordrecht: Kluwer Academic Publishers.
Knapp, M., Baehtz, C., Ehrenberg, H. & Fuess, H. (2004). *J. Synchroron Rad.* **11**, 328–334.
Langford, J. I., Cernik, R. J. & Louer, D. (1991). *J. Appl. Cryst.* **24**, 913–919.
McCusker, L. B., Von Dreele, R. B., Cox, D. E., Louer, D. & Scardi, P. (1999). *J. Appl. Cryst.* **32**, 36–50.
Masson, O., Dooryhée, E., Cheary, R. W. & Fitch, A. N. (2001). *Mater. Sci. Forum*, **300**, 378–381.
Masson, O., Dooryhée, E. & Fitch, A. N. (2003). *J. Appl. Cryst.* **36**, 286–294.
Masson, O., Guinebretiere, R. & Dauger, A. (2001). *J. Appl. Cryst.* **34**, 436–441.
Patterson, B. D., Abela, R., Auderset, H., Chen, Q., Fauth, F., Gozzo, F., Ingold, G., Kühne, H., Lange, M., Maden, D., Meister, D., Pattison, P., Schmidt, Th., Schmitt, B., Schulze-Briese, C., Shi, M., Stampanoni, M. & Willmott, P. R. (2005). *Nucl. Instrum. Methods Phys. Res. Sect. A*, **540**, 42–67.
Rietveld, H. (1969). *J. Appl. Cryst.* **2**, 65–71.
Rodriguez-Carvajal, J. (1993). *Physica B*, **192**, 55.
Sabine, T. M. (1987). *J. Appl. Cryst.* **20**, 23–27, 173–178.
Scardi, P., Leoni, M., Cappuccio, G., Langford, J. I. & Cernik, R. J. (1996). *Mater. Sci. Forum*, **228**, 207–212.
Scherrer, P. (1918). *Gött. Nachr.* **2**, 98–100.

Schmitt, B., Bröennimann, Ch., Eikenberry, E. F., Hülsen, G., Toyokawa, H., Horisberger, R., Gozzo, F., Patterson, B., Schulze-Briese, C. & Tomikazi, T. (2004). *Nucl. Instrum. Methods Phys. Res. Sect. A*, **518**, 436–439.

Stampanoni, M., Bocher, G., Wyss, P., Abela, R., Patterson, B., Hunt, S., Vermeulen, D. & Rüegsegger, P. (2002). *Nucl. Instrum. Methods Phys. Res. Sect. A*, **491**, 291–301.

Susini, J. (1995). *Opt. Eng.* **34**, 361–376.

Thompson, P., Cox, D. E. & Hastings, J. B. (1987). *J. Appl. Cryst.* **20**, 79–83.

Toraya, H., Hibino, H. & Ohsumi, K. (1996). *J. Synchrotron Rad.* **3**, 75–83.

Willmott, P. R., Schlepuetz, C. M., Patterson, B. D., Herger, R., Lange, M., Meister, D., Maden, D., Bröennimann, Ch., Eikenberry, E. F., Hülsen, G. & Al-Adwan, A. (2005). *Appl. Surf. Sci.* **247**, 188–196.